Part 5
Alternate Sound Field Separation Method — Double Concentric Layers Measurement

Concentric Layers Measurement SFS — The Basics

Recall equation 4.1:

$$\hat{p}(r,\theta,\phi;\omega) = \sum_{n=0}^{N}\sum_{m=-n}^{n}\left[C_{mn}h_n^{(1)}(kr) + D_{mn}j_n(kr)\right]Y_n^m(\theta,\phi) \tag{4.1}$$

When all measurements are taken at the same $r = r_1$ (which means they are all taken on a spherical surface of radius r_1 centered to the coordinate system origin) the terms $C_{mn}h_n^{(1)}(kr_1) + D_{mn}j_n(kr_1)$ are functions only of m and n and are combined into α_{mn}. (Note that α_{mn} is only valid for $r = r_1$.)

Similarly, with a second measurement at $r = r_2$ (i.e. on a concentric spherical surface of different radius) and at the identical angular coordinates, we will obtain $\beta_{mn} = C_{mn}h_n^{(1)}(kr_2) + D_{mn}j_n(kr_2)$. Putting the two together, we have:

$$\hat{p}(r_1,\theta,\phi;\omega) = \sum_{n=0}^{N}\sum_{m=-n}^{n}\left[C_{mn}h_n^{(1)}(kr_1) + D_{mn}j_n(kr_1)\right]Y_n^m(\theta,\phi) = \sum_{n=0}^{N}\sum_{m=-n}^{n}\alpha_{mn}Y_n^m(\theta,\phi)$$
$$\hat{p}(r_2,\theta,\phi;\omega) = \sum_{n=0}^{N}\sum_{m=-n}^{n}\left[C_{mn}h_n^{(1)}(kr_2) + D_{mn}j_n(kr_2)\right]Y_n^m(\theta,\phi) = \sum_{n=0}^{N}\sum_{m=-n}^{n}\beta_{mn}Y_n^m(\theta,\phi)$$

By equating terms:

$$\alpha_{mn} = C_{mn}h_n^{(1)}(kr_1) + D_{mn}j_n(kr_1)$$
$$\beta_{mn} = C_{mn}h_n^{(1)}(kr_2) + D_{mn}j_n(kr_2)$$

Written in matrix form:

$$\begin{bmatrix}\alpha_{mn}\\ \beta_{mn}\end{bmatrix} = \begin{bmatrix}h_n^{(1)}(kr_1) & j_n(kr_1)\\ h_n^{(1)}(kr_2) & j_n(kr_2)\end{bmatrix}\begin{bmatrix}C_{mn}\\ D_{mn}\end{bmatrix}$$
$$\Rightarrow \quad \begin{bmatrix}C_{mn}\\ D_{mn}\end{bmatrix} = \begin{bmatrix}h_n^{(1)}(kr_1) & j_n(kr_1)\\ h_n^{(1)}(kr_2) & j_n(kr_2)\end{bmatrix}^{-1}\begin{bmatrix}\alpha_{mn}\\ \beta_{mn}\end{bmatrix} \tag{5.1}$$
$$= \frac{1}{h_n^{(1)}(kr_1)j_n(kr_2) - j_n(kr_1)h_n^{(1)}(kr_2)}\begin{bmatrix}j_n(kr_2) & -j_n(kr_1)\\ -h_n^{(1)}(kr_2) & h_n^{(1)}(kr_1)\end{bmatrix}\begin{bmatrix}\alpha_{mn}\\ \beta_{mn}\end{bmatrix}$$

We can use least squares to solve for α_{mn} and β_{mn}, and use equation 5.1 to solve for C_{mn} and D_{mn}. The same techniques as described in earlier parts can then be used for sound field separation and sound field reconstruction.

However, when $h_n^{(1)}(kr_1)j_n(kr_2) - j_n(kr_1)h_n^{(1)}(kr_2) = 0$, the system of equations in equation 5.1 becomes singular and no solution to C_{mn} and D_{mn} can be found. Analysis by Li et

al. [1, Section 1.4] indicated that the singularity can be avoided by limiting the separation distance d to much less than the wavelength, i.e. $d = |r_1 - r_2| \ll \lambda$. Garcia et al. [2, Section 2.1] recommended limiting d to less than half the wavelength of the highest frequency of interest.

For simplicity, the linear equation solver `numpy.linalg.solve()` is used in the Python code for the simulations to solve for α_{mn} and β_{mn} in equation 5.1. This should also be faster than calculating using the analytical solution given in equation 5.1 as significantly fewer computations would have to be handled by interpreted execution.

A Quick Note on the Coefficient Indices

In the computer code, the coefficients α_{mn} and β_{mn} are usually stored and processed as 1-D arrays (to represent these coefficients as column vectors). It is therefore desirable to express the indices m and n as a single index $j = n^2 + n + m$:

$$\sum_{n=0}^{N} \sum_{m=-n}^{n} \alpha_{mn} Y_n^m(\theta, \phi) \equiv \sum_{j=0}^{(N+1)^2} \alpha_j \Psi_j(\theta, \phi)$$

$$\begin{aligned} \text{where:} \qquad \alpha_j &= \alpha_{mn} \\ \Psi_j(\theta, \phi) &= Y_n^m(\theta, \phi) \\ j &= n^2 + n + m \end{aligned}$$

Simulations

The simulations in Parts 2 and 3 were all performed with simulated measurements at about 1 m from the center of our spherical coordinate system (randomly distributed between 0.95 m and 1.05 m to be exact). The subsequent pressure reconstructions were made on a spherical surface 1 m from the center. In retrospect this choice of reconstruction grid was not a good one. All the measurement and reconstruction points had very similar values for their r coordinates. This did not allow for a proper assessment of the reconstruction accuracy of in the r-direction, especially when our goal is to reconstruct at the ANSI/CTA-2034-A spinorama grid of 2 m radius.

In this part of the report the pressure reconstructions were performed on a flat hollow circular disc grid on the xy-plane (the horizontal plane). The inside radius of the reconstruction grid is equal to the radius of the outermost measurement point. Pressure reconstructions at locations inside of the measurement surfaces are *inverse problems*—an attempt to find out what the sound wave was before it reached the measurement locations. This type of problems is mathematically ill-posed. Errors in the solutions scale inversely to the ratio of reconstruction radii to measurement radii [3, Chapter 3.4]. For us, we are only concerned with sound pressure reconstructions further away from our measurement locations. Our reconstruction grid therefore starts at the radius of the outermost measurement point. The outside radius of the reconstruction grid in the examples is 2.25 m—slightly beyond the spinorama radius. To more closely represent real measurements, the simulated measurement grid radii were reduced to about 0.75 m.

Data Visualization

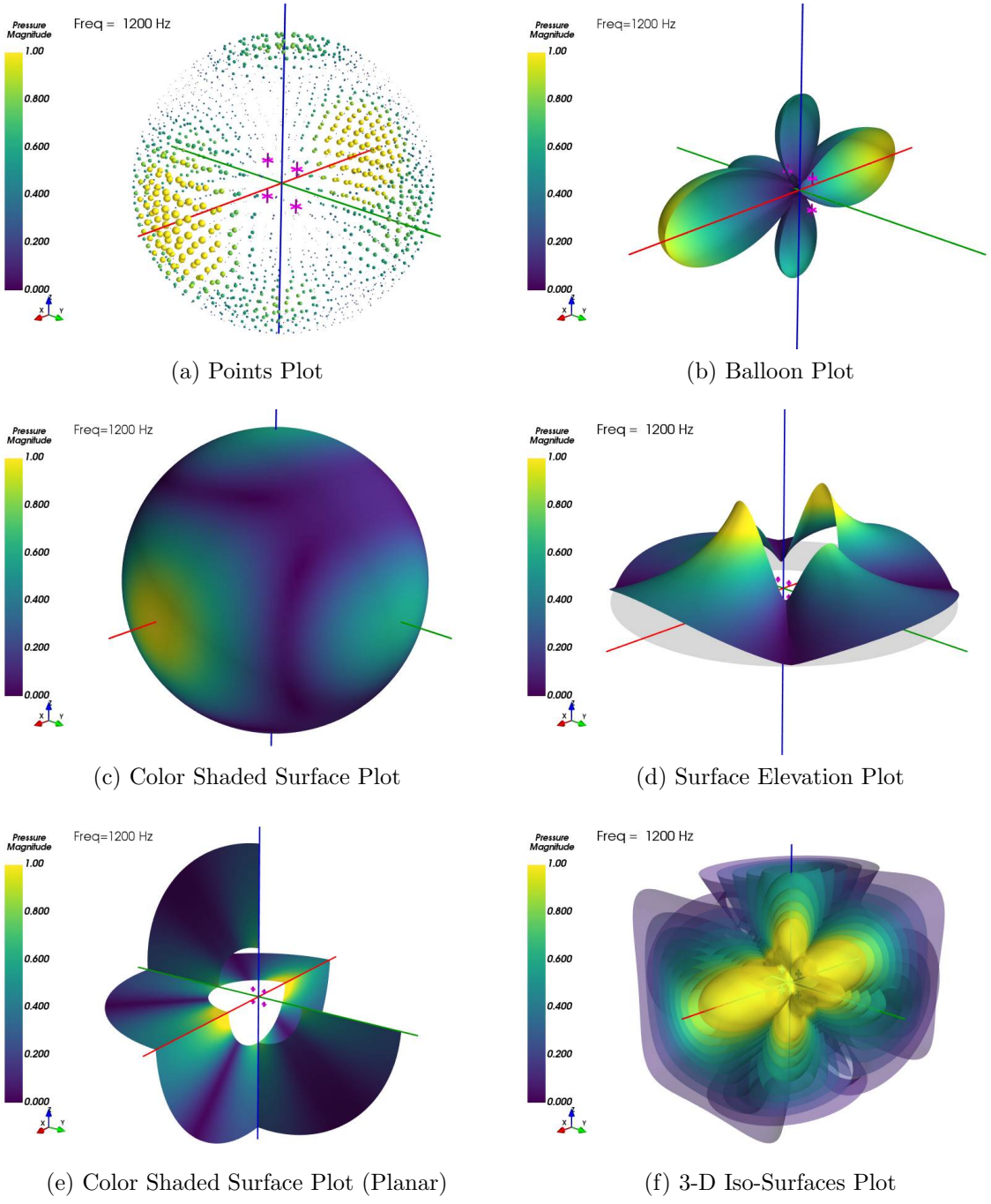

(a) Points Plot

(b) Balloon Plot

(c) Color Shaded Surface Plot

(d) Surface Elevation Plot

(e) Color Shaded Surface Plot (Planar)

(f) 3-D Iso-Surfaces Plot

Figure 1: Multiple Ways to Visualize the Sound Pressure Field from the Same Sources

There are probably uncountable numbers of ways to visualize a 3-D sound pressure field. Figure 1 shows six. All 6 plots show the pressure field radiated by the same simulated sound sources—which are indicated by the 3-D magenta crosses.

(a) Figure 1(a) shows the double concentric measurement grid points as color shaded spheres, with the sphere diameters scaled to the pressure magnitudes.

(b) Figure 1(b) shows a balloon plot of the pressures at a spherical surface 1 m from the center—the same way as they were presented in the Parts 2 and 3 simulations. The r-coordinates of the balloon are proportional to the pressure magnitudes.

(c) Figure 1(c) shows the identical pressures as 1(b) using a surface plot. The actual "measurement" surface is shown, with the pressure magnitudes indicated by color shading.

(d) Figure 1(d) shows the pressure magnitudes on the xy-plane. The elevation (z values) of the surface is proportional to the pressure magnitude. The light gray "shadow" gives the footprint of the "measurement" surface.

(e) Figure 1(e) shows the pressure magnitudes on the xy, yx and xz planes as color shaded surfaces.

(f) Figure 1(f) shows the equi-pressure iso-surfaces in 3-D.

Since we will be assessing the pressure reconstruction performance using a planar grid on the xy plane, balloon plots are not applicable and surface elevation plots as shown in Figure 1(d) are used to present the simulation results.

Reconstruction with Concentric Measurements

In part 3, using the "aspherical" grid measurement method at 2000 Hz, we needed 7082 measurements to reconstruct with sound field separation. Figure 2 shows the results with approximately 2000 measurements using a concentric double layer measurement grid.

The measurement grid (see figure 1(a)) is made up of two layers of evenly spaced points. The angular coordinates of all the points on the two layers matched each other exactly. The radius of the outer grid is 0.75 m. The separation between the two grids is 90% of the half wavelength of a 3000 Hz sound wave.

Figure 2(a) to (c) show the reference pressure fields with both internal and external sources, internal sources only, and external sources only. Figure 2(d) to (f) show the reconstructions with order $N = 4$, figure 2(g) to (i) show the reconstructions with order $N = 12$, and figure 2(j) to (l) show the reconstructions with order $N = 27$. The internal and external sources reconstructions were performed with sound field separations (SFS). Satisfactory reconstruction using SFS to separate out the internal sources was obtained at a much lower expansion order N than when aspherical measurements were used in Part 3. It can be seen that the reconstructions of mixed sources and external sources only were not as satisfactory. The reason is the external sources were very far from the origin of our spherical wave expansion functions, and they will require very high order expansion functions and significantly more measurements to be well captured. However, it can also be seen that we are able to reconstruct the internal sources with fairly low orders. This is very much opposite to the results of the aspherical measurement method, where the internal sources SFS reconstructions were less accurate than the mixed sources reconstructions.

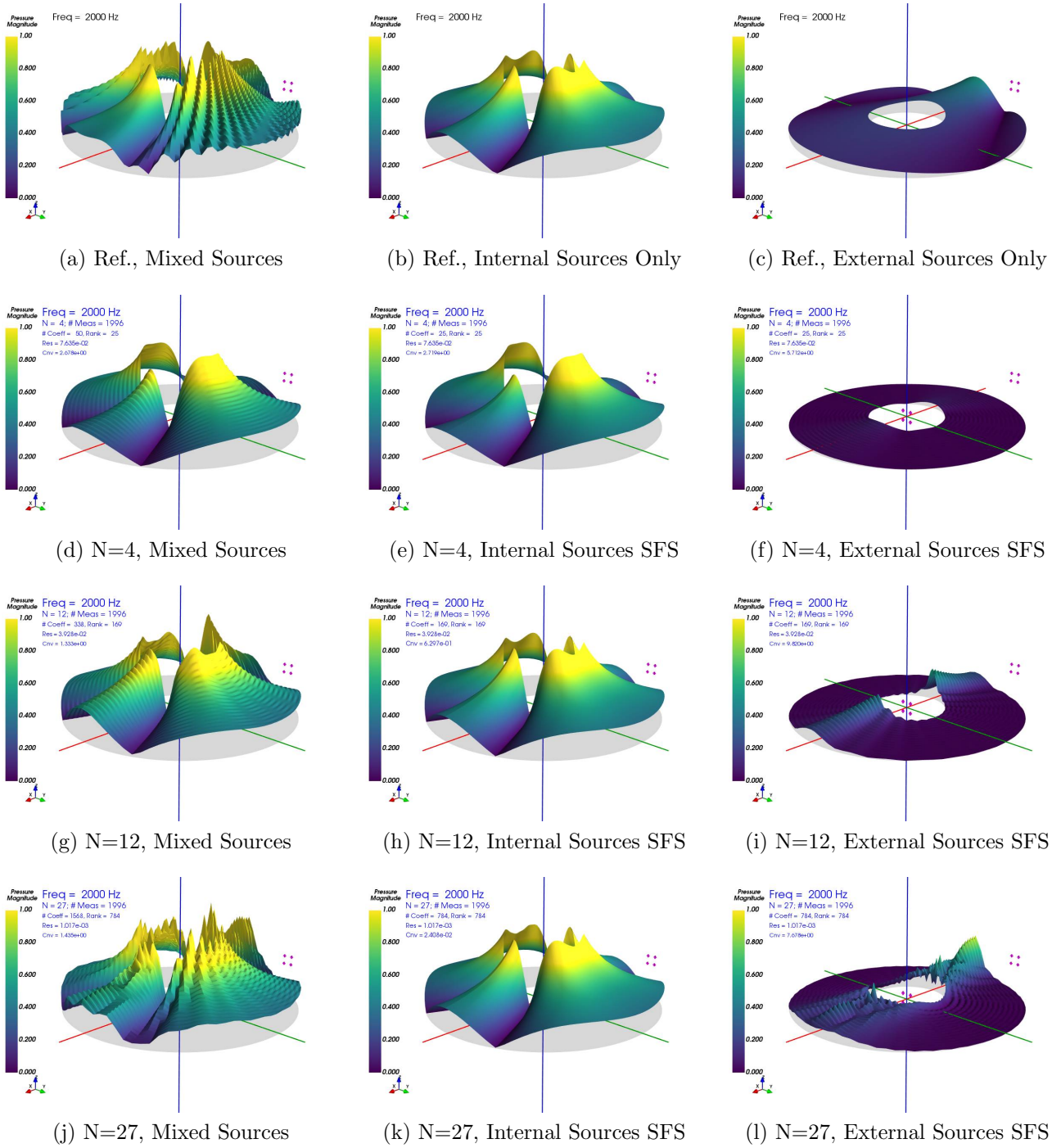

(a) Ref., Mixed Sources (b) Ref., Internal Sources Only (c) Ref., External Sources Only

(d) N=4, Mixed Sources (e) N=4, Internal Sources SFS (f) N=4, External Sources SFS

(g) N=12, Mixed Sources (h) N=12, Internal Sources SFS (i) N=12, External Sources SFS

(j) N=27, Mixed Sources (k) N=27, Internal Sources SFS (l) N=27, External Sources SFS

Figure 2: Double Concentric Layers Reconstruction, 2000 Hz, 1996 Measurements

Figure 3 shows the plots of the least squares residuals, the convergence metrics, the maximum and mean reconstruction errors against the expansion function order for the three reconstruction cases. We are most interested in figure 3(b).

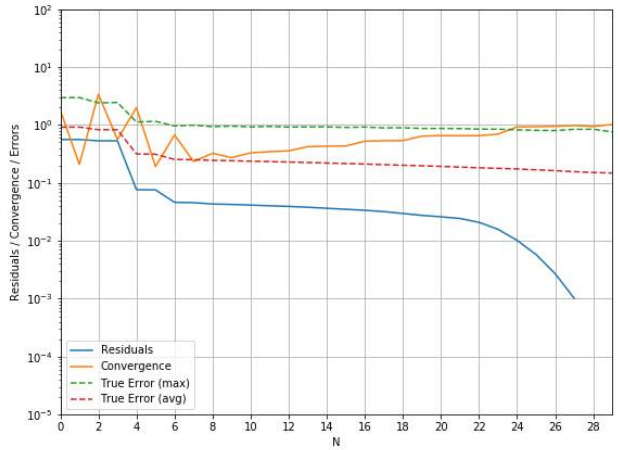

(a) Mixed Sources Reconstruction

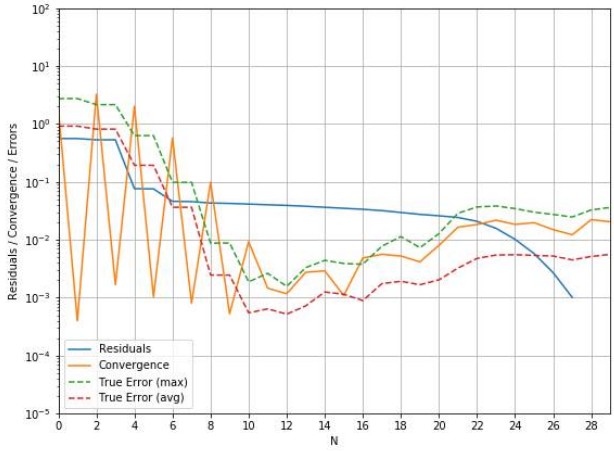

(b) Internal Sources SFS Reconstruction

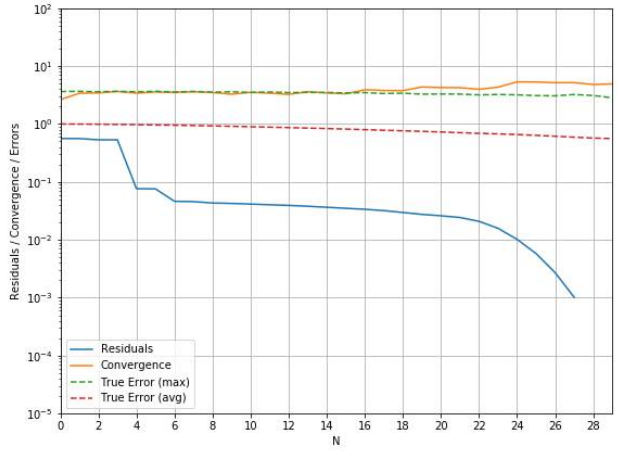

(c) External Sources SFS Reconstruction

Figure 3: Plots of the Least Squares Residuals, Convergence Metrics, and True Errors Against the Expansion Order N

The least squares residuals decrease monotonously with N. This is not a surprise as this is how least squares work. However, we can see that the residuals do not track the true errors. The convergence metric is computed by calculating the differences in the reconstruction solutions between the current order ($N = n$) and the previous order ($N = n - 1$). The maximum difference is then normalized to the mean magnitude of the solution with the current order ($\varepsilon = \max|\hat{p}_{N=n} - \hat{p}_{N=n-1}|/\text{mean}|\hat{p}_{N=n}|$). The true errors are calculated similarly but is referenced against the theoretical solution. Both maximum and mean are shown.

From figure 3, we can see that the convergence metrics track the true errors well. In particular for the internal sources case (figure 3(b)), the true errors and convergence metrics

follow the typical U-shaped curves where they decrease initially, reach a minimum, and then increase again as the least squares method starts to overfit. The convergence metrics can be used to determine the optimal expansion order $N_{optimal}$.

Figure 4 shows the SFS reconstruction errors up to 3000 Hz.

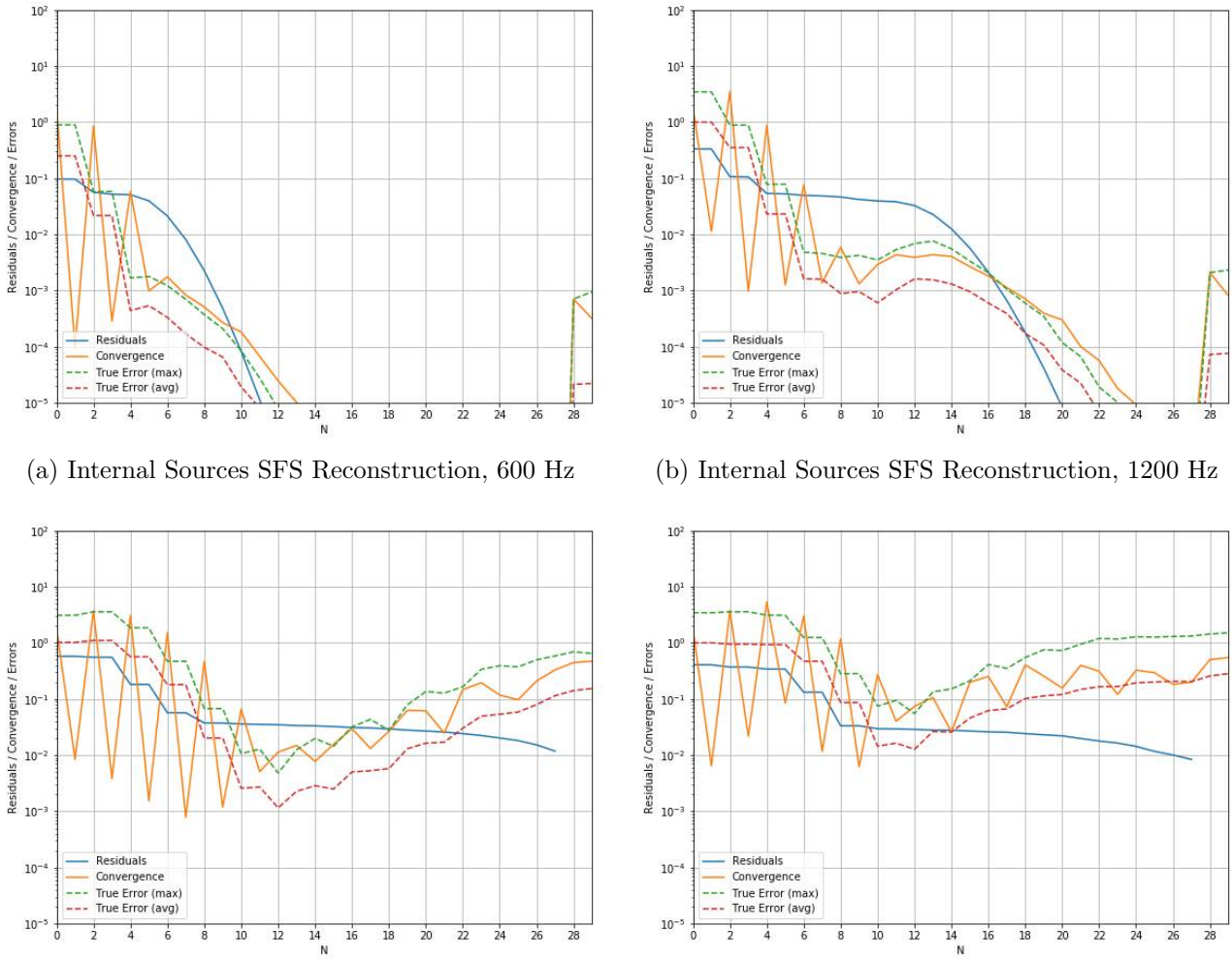

(a) Internal Sources SFS Reconstruction, 600 Hz

(b) Internal Sources SFS Reconstruction, 1200 Hz

(c) Internal Sources SFS Reconstruction, 2500 Hz

(d) Internal Sources SFS Reconstruction, 3000 Hz

Figure 4: Error Plots for SFS Reconstructions at 600 Hz, 1200 Hz, 2500 Hz and 3000 Hz

References

[1] WeiBing Li, MeiZhuan Lian, ChuanXing Bi, Jian Chen and XinZhao Chen, Separation Theory of the Incident and Scat- tered Sound Fields in Spherical Coordinate, Science in China Series E: Technological Sciences, Science in China Press, Springer-Verlag 2007

[2] A. Garcia, Y. Braïkia, C. Langrenne, É. Bavu, M. Melon. Source identification in small spaces using field separation method: Application to a car trunk. Proceedings of Acoustics2012, Nantes, France, April 23-27, 2012

[3] S. F. Wu, The Helmholtz Equation Least Squares Method, Springer Science+Business Media New York 2015